Numerical and experimental investigation of the axis-switching behavior of a rectangular jet

García Llamas, C.; Swami, V. V.; Petrova, V. P.; Buist, K. A.; Kuipers, J. A.M.; Baltussen, M. W.

DOI
10.1016/j.ijmultiphaseflow.2024.104951

Publication date
2024

Document Version
Final published version

Published in
International Journal of Multiphase Flow

International Journal of Multiphase Flow 180 (2024) 104951

Contents lists available at ScienceDirect

International Journal of Multiphase Flow

journal homepage: www.elsevier.com/locate/ijmulflow

Numerical and experimental investigation of the axis-switching behavior of a rectangular jet

C. García Llamas [a], V.V. Swami [a], V.P. Petrova [a,b], K.A. Buist [a], J.A.M. Kuipers [a], M.W. Baltussen [a,*]

[a] Department of Chemical Engineering and Chemistry, Multiphase Reactors Group, Eindhoven University of Technology, P.O. Box 513, 5600 MB Eindhoven, The Netherlands

[b] Delft University of Technology, Process and Energy department, Multiphases System group, Leeghwaterstraat 39, 2628 CB Delft, The Netherlands

ARTICLE INFO

Keywords:
Numerical simulation
Rectangular jet
Axis-switching
Local Front Reconstruction Method

ABSTRACT

Rectangular jets exhibit axis-switching behavior which results in enhanced flow entrainment compared to round jets. This feature allows for their potential industrial use as passive flow controllers in mixing applications. However, rectangular jets have received limited attention compared to round jets. To operate rectangular jets optimally, a better understanding on the underlying phenomena influencing the axis-switching of the jet is required. In this paper, Direct Numerical Simulations of rectangular jets are performed at different injection velocities using the Local Front Reconstruction Method (LFRM) to track the liquid–gas interface. The simulations are validated using experiments in a similar range of Weber and Reynolds numbers. The obtained results showed that LFRM can accurately capture the jet oscillations, break-up lengths and droplet sizes observed experimentally. Additionally, a fully developed velocity profile at the nozzle outlet enhances the jet stability resulting in larger break-up length values compared to a uniform velocity profile.

1. Introduction

Liquid jet break-up is crucial in industrial processes such as liquid fuel injection and combustion, agriculture crop spraying, granulation, coating, and ink-jet printing (Lekic and Birouk, 2009; Eggers and Villermaux, 2008). In these applications, the jet emerging from an orifice breaks due to the effect of disrupting instabilities. The rate of growth and decay of these instabilities is determined by multiple factors: surface tension, inertia, aerodynamic effects, velocity profile relaxation, viscous dissipation, turbulence or the nozzle geometry (Lekic and Birouk, 2009). In particular, the geometrical properties of the nozzle, such as surface roughness, nozzle aspect ratio or contraction angle, are critical in the jet stability (McCarthy and Molloy, 1974). Additionally, non-circular orifice shapes enhance the flow entrainment (Gutmark and Grinstein, 1999), which make non-circular jets suitable as passive flow control systems. Despite this, non-circular jets are less studied in comparison with round jets (Rayleigh, 1878; Reitz and Bracco, 1986; Lekic and Birouk, 2009). The first observation of the behavior of non-circular jets was made by Bidone (1829), who observed the alternating switching of the jet cross-section along its moving direction, which is labeled as the axis-switching behavior of the jet. Later, Magnus (1855) observed axis-switching in triangular, rectangular and square jets, which Rayleigh et al. (1879) described using linear theory. Since then, several authors have investigated the axis-switching behavior of non circular jets, mainly on ellipsoidal orifices (Husain and Hussain, 1983; Ho and Gutmark, 1987; Amini and Dolatabadi, 2011, 2012; Farvardin and Dolatabadi, 2013). These investigations confirmed that axis-switching of a non-circular jet is mainly influenced by the effect of a non uniform azimuthal curvature and the interaction between the streamwise and azimuthal vortices (Gutmark and Grinstein, 1999; Koshigoe et al., 1989; Ho and Gutmark, 1987; Husain and Hussain, 1993; Kasyap et al., 2009). These non-circular orifices generally enhance the instability of the jet leading to shorter break-up lengths compared to round jets (Wang and Fang, 2015). Both elliptic and rectangular orifices exhibit axis-switching behavior where the jet expands and contracts along the major and minor diagonals of the orifice. However, rectangular jets are significantly less investigated than elliptic jets (Husain and Hussain, 1983; Ho and Gutmark, 1987; Amini and Dolatabadi, 2011) due to the complexity introduced by its sharp geometry which influences the deformation of the vortical structures, and therefore, the flow entrainment. The experimental works of Wang and Fang (2015), Tadjfar and Jaberi (2019) and Jaberi and Tadjfar (2019) revealed that rectangular jets have shorter break-up lengths compared to other non-round orifices and exhibit the axis-switching deformations for a broad range of aspect ratios and ejecting pressures. More recently, Straccia and Farnsworth (2021) studied the interaction of the vortex rings with the axis-switching behavior for low

* Corresponding author.
E-mail address: m.w.baltussen@tue.nl (M.W. Baltussen).

https://doi.org/10.1016/j.ijmultiphaseflow.2024.104951
Received 1 May 2024; Received in revised form 21 July 2024; Accepted 2 August 2024
Available online 8 August 2024

and moderate aspect ratio nozzles. Besides the experimental studies, rectangular and ellipsoidal jets have been investigated numerically. For example, Chen and Yu (2014) described the axis-switching behavior of rectangular jets using a Lattice Boltzmann Method (LBM) to capture the interface. Morad et al. (2020) reproduced the experimental work of Wang and Fang (2015) using a Volume of Fluid method (VOF) to represent the interface. Farvardin and Dolatabadi (2013) simulated elliptical jets using VOF in combination with a Large Eddy Simulation (LES) approach, and validated the method with the experiments of Kasyap et al. (2009). Rectangular jets with a significantly larger scale compared to those investigated in this work have also been studied by Carrillo et al. (2021b,a) and Castillo et al. (2015, 1999) in the field of hydraulic structures. Despite these research efforts, the physical mechanisms influencing the interaction between vortical structures and the axis-switching of rectangular jets have not been fully described.

As evident from the review above, most of the numerical studies focused on rectangular jet break-up using VOF, which is a front capturing technique that tracks the interface using a color function (Van Sint Annaland et al., 2005). Front capturing techniques are widely used for simulating multi-phase flows as these methods can capture the evolution of the interface topology (i.e, merging or break-up of interfaces). However, to capture the small scale deformations at the interface these front capturing methods require a high level of grid refinement (i.e., very small computational cells). In contrast, the Front Tracking methods (Dijkhuizen et al., 2010; Shin et al., 2011) represent the interface with Lagrangian markers that are moved with the local velocity interpolated from the Eulerian velocity fields. Due to the sub-grid representation of the interface, front tracking methods reduce the required Eulerian grid resolution compared to front capturing techniques. However, traditional Front Tracking methods cannot handle the large topological changes due to the numerical complexity of maintaining the marker points connectivity. To allow merging and break-up while keeping the sharp representation of the interface, the Local Front Reconstruction Method (LFRM) (Shin et al., 2011) is used in this work to represent the gas-liquid interface. LFRM is a Front Tracking technique that does not require local connectivity of the markers and therefore enables handling of merging and break-up in a simpler manner compared to the traditional Front Tracking methods.

In this work, we demonstrate the capabilities of LFRM by comparing our numerical results with detailed experimental data. Additionally, we study the impact of flow profile at the outlet on the break-up properties (i.e., break-up length and droplet sizes) and the axis-switching behavior of the jet.

This paper is structured as follows: First, the experimental methodology section covers the details of the experimental set-up used in this work followed by an explanation of the numerical method. Subsequently, the features of the simulated jet as well as the associated operating conditions are described. We include a section to address the grid sensitivity of our computational results. Subsequently, the simulation and experimental results are presented and discussed. Finally, the main findings of this research are summarized.

2. Methodology

2.1. Experimental methodology

Experiments were carried out using the experimental set-up schematically shown in Fig. 1. Demineralized water is injected via two syringe pumps (KD Scientific Legato) connected by silicone tubes under a fixed flow rate and atmospheric pressure conditions. This flow rate is defined based on the Reynolds number. Two nozzles with aspect ratios (AR) 5 and 8 are used, of which the geometrical properties are described in Table 1 and Fig. 2. The jet break-up properties are captured using a high speed shadowgraphy technique with two high speed cameras (LaVision SA3) equipped with a Nikon 200 mm f/4 AF-D macro lenses, at $20,000$ fps and at an exposure time of $5\cdot10^{-5}$ s and a resolution of 10.4 px/mm, and 9.2 px/mm for N1, and N2, respectively. The two cameras are placed at a 90° angle to capture the front and side view of the falling jet. To ensure optimal illumination conditions, LED banks are placed behind the diffusion plates to ensure uniform backlighting. Before each run, the nozzles are wiped to eliminate residual droplets from previous runs. Each syringe pump is set to half of the desired flow rate to obtain the desired fluid flow rate. Finally, the experimental images are obtained after a steady and stable flow is observed. A background and scaling image are taken for image analysis.

Table 1
Nozzle dimensions where d_s and d_b, are the cross sectional diameters of the orifice, d_h is the hydraulic diameter, and $L_{dev.}$ the nozzle length.

Nozzle	AR	d_s [μm]	d_b [μm]	d_h [μm]	$L_{dev.}$ [mm]
N1	5	500	2500	833.3	32
N2	8	500	4000	888.9	32

2.1.1. Image analysis

The 2D images are post-processed using MATLAB to obtain relevant break-up properties such as the break-up length, the averaged droplet diameter and the axis-switching oscillations of the jet. The general image processing routine is schematically shown in Fig. 3. First, the images are cropped to the size of the area of interest. Subsequently, the background image is subtracted. To increase the contrast, the obtained image is then multiplied by a factor. Next, the image is binarized using a sensitivity factor. To ensure an optimal definition of the binarized images, the multiplication and binarization factor are adjusted individually for each case. Finally, these binarized images are used to compute the break-up properties of the jet, see Fig. 4.

The jet middle points (see green dots in Fig. 4) are calculated using the top left, top right, bottom left, and bottom right of the jet (see red dots in Fig. 4), which are computed with the *regionprops* function from MATLAB. Finally, the break-up length is calculated as the distance between the middle points (see green line in Fig. 4). The jet radial oscillations are calculated using the *bwboundaries* function from MATLAB (see red line in Fig. 4), which are stored separately for the left and right side of the jet. To reduce noise in the image, points located at the same height are averaged. Finally, the radial oscillations are time-averaged using the computed jet radial oscillations per frame. To characterize the wavelengths of the oscillations, the time-averaged radial position of the jet is interpolated with the *fit* function from MATLAB. Then, the wavelengths and the amplitude of oscillations are computed using the *findpeaks* function. The break-up length and radial oscillations are normalized by the hydraulic diameter of the nozzle. Finally, the averaged droplet diameter is computed using the *equivalent diameter* property evaluated with the *regionprops* function. In the experimental images of the jet with $AR = 8$ (see geometrical specifications in Table 1) a shadow is observed just underneath the nozzle outlet which is regarded as the actual nozzle outlet by the post-processing script (see Fig. 5). To correct for this, the obtained position of the jet is adjusted by adding an offset computed as the length of the shadow area (approximately 7 pixels).

2.2. Numerical methodology

2.2.1. Governing equations

In this work, a one fluid formulation is adopted where the equations for the liquid and gas phase are combined, see Eqs. (1) and (2).

$$\nabla\cdot\mathbf{u}=0, \tag{1}$$

$$\rho\frac{\partial\mathbf{u}}{\partial t}+\rho\nabla\cdot(\mathbf{uu})=-\nabla p+\rho\mathbf{g}-\nabla\cdot\boldsymbol{\tau}+\mathbf{F}_{\sigma}, \tag{2}$$

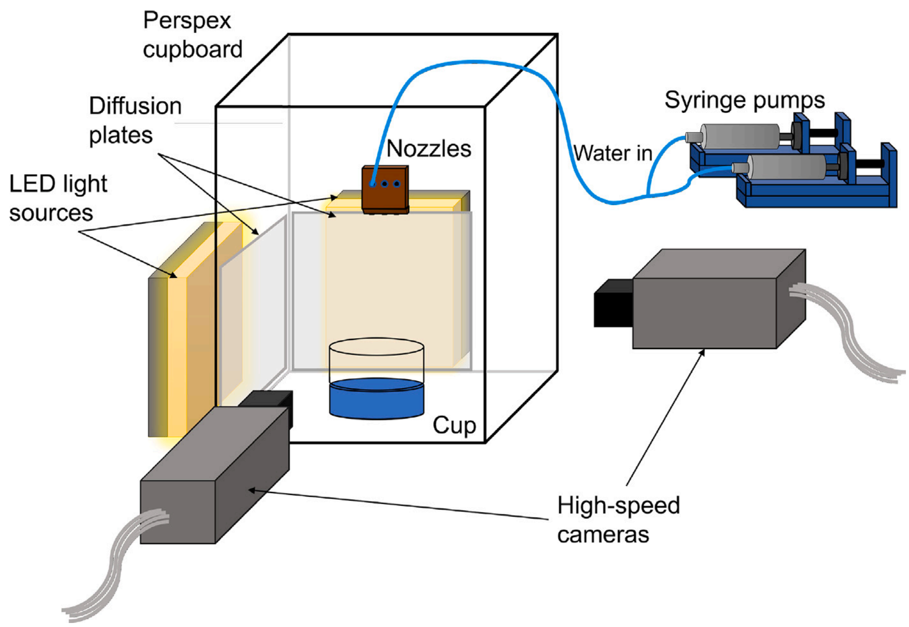

Fig. 1. Schematic representation of the experimental setup.

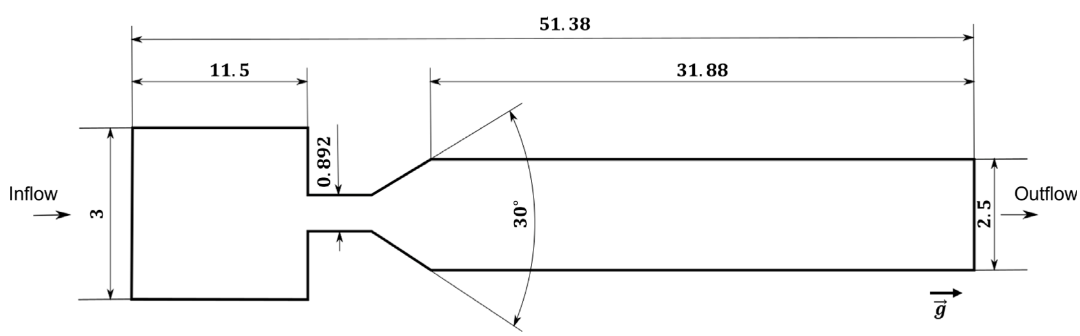

Fig. 2. Sketch of the nozzle design, where the dimensions are in mm.

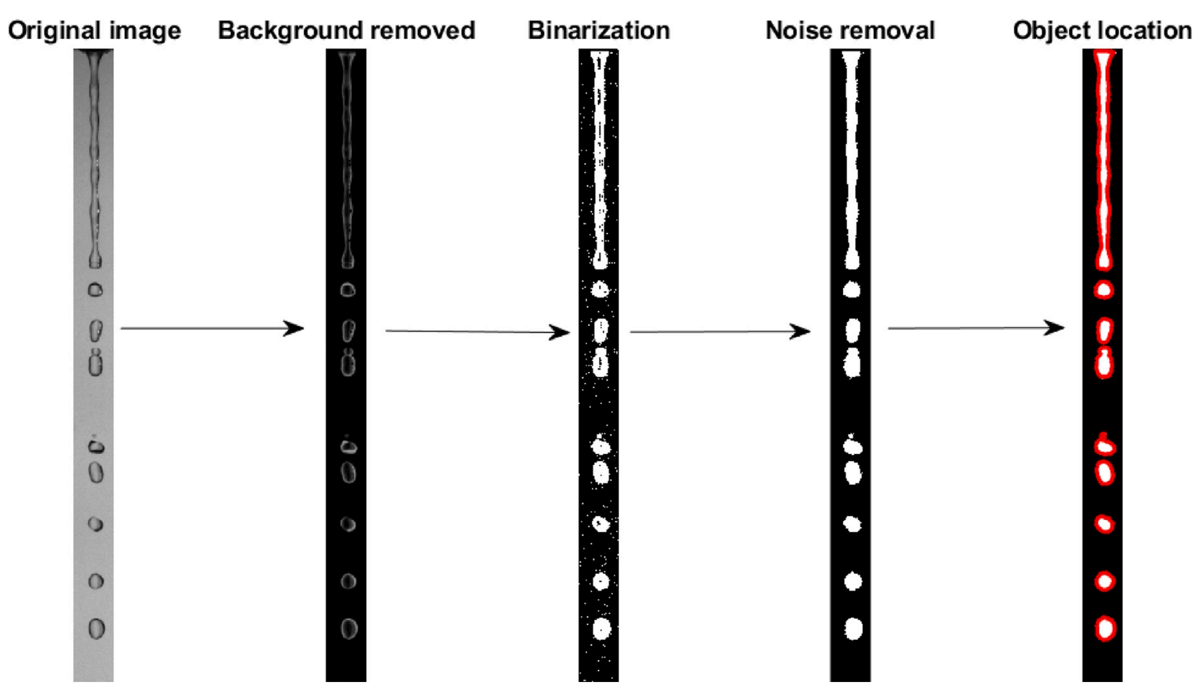

Fig. 3. Image treatment steps.

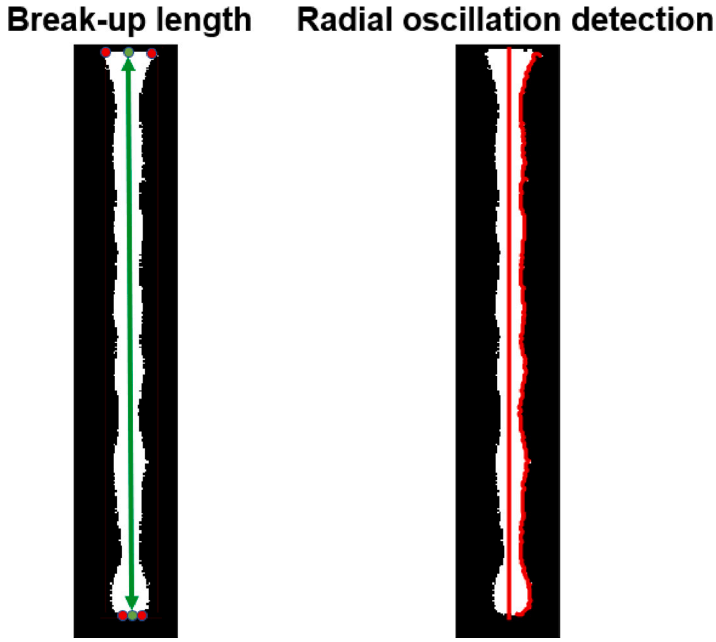

Fig. 4. Image analysis methods: Break up length (left) and radial oscillations (right). (For interpretation of the references to color in this figure legend, the reader is referred to the web version of this article.)

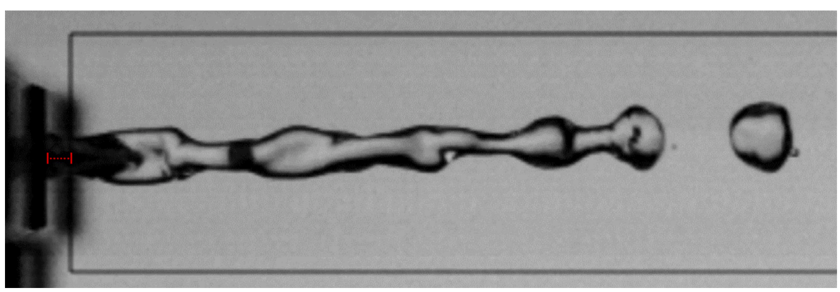

Fig. 5. Experimental image of the jet with $AR = 8$ with a shadow underneath the nozzle outlet. The red line indicates the length of the shadowed area.

where ρ is the density, $\mathbf{u}$ the fluid velocity, t the time, p the pressure, $\mathbf{g}$ the gravity, and $\boldsymbol{\tau}$ the stress tensor given by $-\mu\left[\nabla\mathbf{u}+(\nabla\mathbf{u})^T\right]$. The density and viscosity are calculated each time step by simple linear and harmonic averaging of the phase fraction field, respectively.

The surface tension force is represented by $\mathbf{F}_\sigma$, which is computed using the pull force method of Dijkhuizen et al. (2010). The tensile force exerted by a neighboring marker on a given marker is computed using Eq. (3) (Deen et al., 2004).

$$\mathbf{F}_{\sigma,(i,m)} = \sigma(\mathbf{t}_{i,m} \times \mathbf{n}_{edge}), \tag{3}$$

where $t_{i,m}$ is the shared tangent of a marker i and m and $\mathbf{n}_{edge}$ the normal of the tangent between markers i and m. The overall force exerted on a marker is then calculated with Eq. (4), which is then transferred to the Eulerian grid using a mass-weighting mapping.

$$\mathbf{F}_\sigma = \frac{1}{2\Delta V}\sum_m D(\bar{x}-\bar{x}_m)\sum_{i=1}^{3}\sigma(\bar{t}_{m,i}\times\bar{n}_i). \tag{4}$$

Eqs. (1) and (2) are discretized in a Cartesian staggered grid and solved using a finite volume method approach and the projection method Chorin (1968). With this method, the velocity and pressure are calculated sequentially. First, an initial guess of the velocity ($\mathbf{u}^*$) is computed using Eq. (5).

$$\mathbf{u}^* = \mathbf{u}^\mathbf{n} + \frac{\Delta t}{\rho^n}\left[-\rho^n\nabla\cdot(\mathbf{u}^*\mathbf{u}^*) - \nabla p^n + \rho^n\mathbf{g} - \nabla\cdot\boldsymbol{\tau} + \mathbf{F}_\sigma\right]. \tag{5}$$

The convective term in Eq. (5) is discretized using the minmod Total Variation Diminishing scheme (TVD) (Versteeg and Malalasekera, 1995) and the shear stress is discretized semi-implicitly using a second order differencing scheme.

The tentative velocity obtained after solving Eq. (5) is not mass conservative. To satisfy Eq. (1), the velocity field is adjusted with a correction factor δp computed after solving the Poisson equation in Eq. (6).

$$\nabla\cdot\left[\frac{\Delta t}{\rho^n}\nabla(\delta p)\right] = -\nabla\cdot\mathbf{u}^*, \tag{6}$$

where the pressure correction is defined as $\delta p = p^{n+1} - p^n$. Finally, the velocity is recalculated using the corrected pressure field (see Eq. (7)).

$$\mathbf{u}^{n+1} = \mathbf{u}^* - \frac{\Delta t}{\rho^n}\Delta p^{n+1} \tag{7}$$

The matrix is solved using an AMG-preconditioned of Trilinos Project Team (2020) and the Bi-Conjugate-Gradient stabilized solver 2 (Masterov, 2019).

The time step is adjusted dynamically to ensure numerical stability based on the Courant–Friedrichs–Lewy (CFL) criterium and the capillary criterium from Brackbill (see Eq. (8)) (Brackbill et al., 1992).

$$\Delta t < \min(\Delta t_{CFL}, \Delta t_\sigma) = \min\left(\frac{\Delta x}{v}, \sqrt{\frac{(\rho_l+\rho_g)\Delta x^3}{4\pi\sigma}}\right). \tag{8}$$

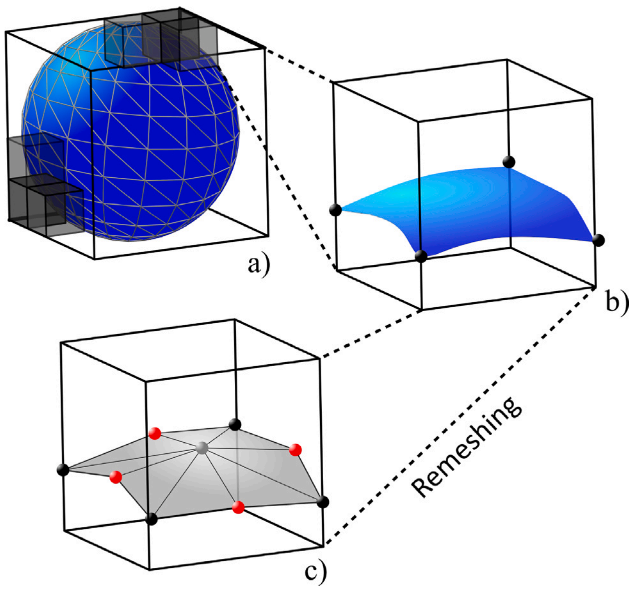

Fig. 6. Schematic representation of the LFRM reconstruction procedure. (a) The interface is intersected by a set of cubic reconstruction cells. (b) The intersections of the interface with the reconstruction cell are calculated (black points). (c) Surface and volume fitting points (red and gray points, respectively) are connected with the edge crossing points. (For interpretation of the references to color in this figure legend, the reader is referred to the web version of this article.)

2.2.2. Interface tracking

The liquid–gas interface is explicitly tracked using Lagrangian marker points. These marker points are connected and form a triangular mesh that moves with the flow field. To evaluate the velocities at the marker point positions, the velocities are interpolated from the cartesian grid to the marker points using cubic spline interpolation. Subsequently, a 4th order explicit Runge–Kutta time integration scheme is used to advanced the marker points. Finally, the phase fraction field is computed using a geometrical procedure where the phase fraction is added or subtracted based on the normal direction of the markers (Dijkhuizen et al., 2010).

The interface advection can cause an uneven distribution of points across the interface, which deteriorates the accuracy of the evaluation of the local surface tension forces. To ensure a homogeneous distribution of points across the interface surface, a remeshing procedure is performed periodically. The technique used in this work is an adaptation of the Local Front Reconstruction Method (LFRM) of Shin et al. (2011). With LFRM, the interface is remeshed following these steps:

1. Localization of the interface: The interface mesh is divided into a grid of reconstruction cells (as shown by the gray shaded cubes in Fig. 6(a)), each of which is half the size of an Eulerian cell.
2. Edge line reconstruction: The points where the interface intersects the edges of the reconstruction cell are determined at each face of the reconstruction cell (see Fig. 6(b)).
3. Surface and Volume reconstruction: Markers are created by connecting the edge crossing points (shown as black points in Fig. 6(c)) with a middle point and a centroid point (shown as red and gray points, respectively, in Fig. 6(c)). The positions of the middle and centroid points are determined through a surface fitting procedure and a volume fitting procedure, respectively.

In the advection and remeshing, numerical discretization errors are introduced that can result in a locally non-smooth interface. To correct for these errors, the smoothing procedure of Kuprat et al. (2001) is performed after the remeshing.

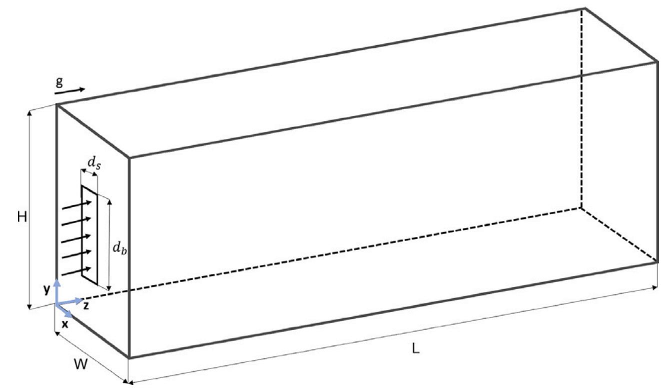

Fig. 7. Computational domain used in this work.

Table 2
Liquid and gas properties used in this research.

Fluid type	Density ρ (kg/m^3)	Viscosity μ (Pa s)	Surface tension σ (N m^{-1})
Water	998.2	$1.001 \cdot 10^{-3}$	$72.8 \cdot 10^{-2}$
Air	1.18	$1.83 \cdot 10^{-5}$	

3. Problem description

In this work, a rectangular jet is simulated corresponding to the computational domain depicted in Fig. 7. The liquid, of which the physical properties are defined in Table 2, is injected into quiescent air through a rectangular orifice centered in $z = 0$, $x = W/2$, and $y = H/2$. The aspect ratio of the orifice AR is defined as the ratio of the length of the major axis to the minor axis ($AR = d_b/d_s$). As LFRM is not capable of handling sharp curvatures in the remeshing (Shin et al., 2011), the rectangular orifice is represented as a super-ellipse (see Eq. (9)), which for exponent values $n > 2$ approximates a rectangle with rounded corners.

$$\left|\frac{x}{r_x}\right|^n + \left|\frac{y}{r_y}\right|^n = 1, \tag{9}$$

where r_x and r_y are the radius across the major and minor diagonal, respectively.

In the present work, an exponent value of $n = 10$ was used as the volume loss caused by the rounded corners was less than 1.3%. The simulations are performed using an uniform Cartesian grid where the length of the lateral direction (H and W in Fig. 7) is $5d_s$ and the length of the injection direction (L in Fig. 7) ranges from $110d_s$ to $140d_s$ for the low and high jet speed, respectively. At the inlet, the velocity is set to the desired value, while a static pressure of 10^5 Pa is used in combination with a Neumann boundary condition at the outlet. A free slip boundary condition is applied to the rest of the domain boundaries. The averaged velocity, U_{avg}, at the inlet is computed on basis of the Reynolds (Re) and Weber (We) numbers, which are expressed according to the following formulas:

$$Re = \frac{\rho_{liq} d_h U_{avg}}{\mu_{liq}}, \tag{10}$$

$$We = \frac{\rho_{liq} d_h U_{avg}^2}{\sigma}, \tag{11}$$

where d_h is the hydraulic diameter, which is computed as $d_h = 4\frac{S_{or}}{l_{or}}$. S_{or} and l_{or} are the area and perimeter of the orifice, respectively, which are computed using the formulas from Wang (2009).

The distance, velocity, time and pressure are transformed into non-dimensional expressions using d_h, U_{avg}, d_h/U_{avg}, and $\rho_w U_{avg}^2$, respectively.

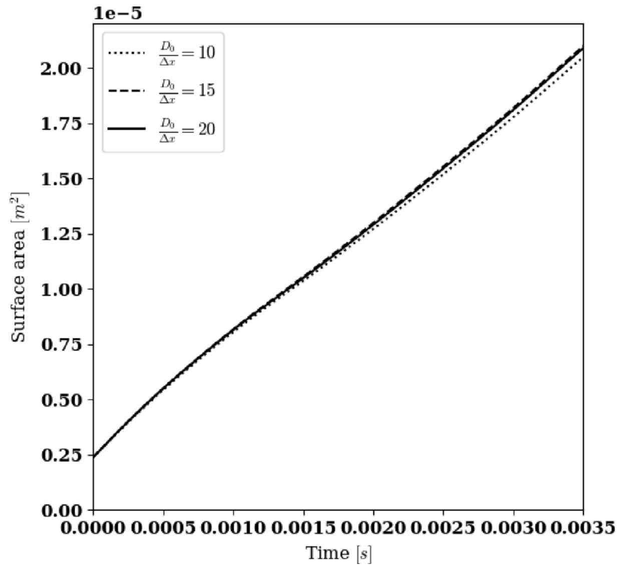

Fig. 8. Surface area of the jet over time.

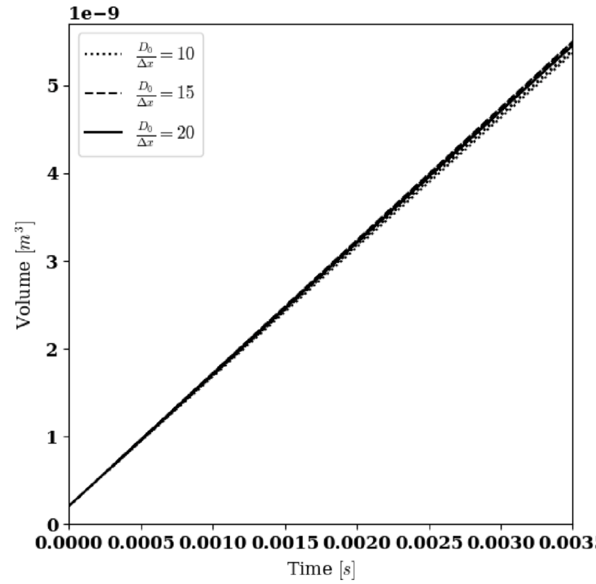

Fig. 9. Jet volume overtime.

In the first part of this paper, the simulations are validated with experimental results. To facilitate this comparison, the rectangular jet simulations are carried out where the jets have the same geometrical properties as the ones used in the experiments (see geometrical properties of the nozzles in Table 1). The velocity profile imposed at the nozzle outlet is a top-hat profile as the entry length is not long enough to achieve a fully develop flow (Wang and Fang, 2015).

In the second part of this work, the effect of a fully develop flow at the nozzle outlet is studied for different injection velocities $Re = (800, 1000, 1200)$. The velocity profile at the nozzle outlet of the super-ellipsoid duct is described using the equation develop by Wang (2009), which is given by the following formula:

$$v_z = \left[1 - \left|\frac{x}{r_x}\right|^n - \left|\frac{y}{r_y}\right|^n\right] Q(x, y), \tag{12}$$

where $Q(x, y)$ is a complete even polynomial in x and y, whose coefficients are computed using the Ritz method. In the present work, a polynomial order of 8 was used as this value is sufficiently high to ensure an accurate representation of the velocity.

4. Grid sensitivity test

A grid sensitivity test was performed to determine the optimal number of cells to simulate a rectangular jet. In this study, three different grid refinements were evaluated with 10, 15 and 20 grid cells across the smallest diameter d_s of the rectangular jet. Figs. 8 and 9 show the surface area and volume of the jet over time, respectively. These graphs evidence that the volume and jet area computed on a coarser grid deviates only slightly from the more refined grids. Thus, a grid resolution of $d_s/\Delta x = 10$ across the small axis of the jet is sufficient for these simulations.

5. Results

Upon injection, the jet exhibits axis-switching behavior, which is evidenced in the alternating expansion and contraction of the jet in two perpendicular planes (see jet oscillations in Fig. 10). In the following sections, the simulated axis-switching behavior and break-up properties of the jet are analyzed and compared with experiments. Subsequently, the effect of the inlet velocity on the break-up and axis-switching properties of the jet is discussed.

5.1. Experimental validation

In this work, we study rectangular jets in a pseudo-stationary regime where the physical and break-up properties are quasi-stationary. Figs. 11 and 12 show the time-averaged jet break-up length and diameter, where the error bars indicate the standard deviation. In these graphs a reasonable agreement is observed between experiments and simulations which evidences that the numerical model can accurately reproduce the break-up properties of rectangular jets for the studied range of We and Re. However, a stronger deviation between the experimental and numerical break-up lengths is observed at $\sqrt{We} = 4.01$ and $Re = 1000$. This discrepancy could be attributed to the different time scales used in the experiments and simulation (i.e., seconds in the experiment and milliseconds in the simulation). In addition to this, the large changes in the numerical break-up length (see Fig. 13) suggests deviations from the pseudo-steady regime, which could lead to an over-prediction of the averaged break-up length. Additionally, the jet elongation increases almost linearly with $\sqrt{We}$ for the experiments, which is consistent with the expected trend in the Rayleigh regime (Tadjfar and Jaberi, 2019). With increasing values of AR, the jet cross-section becomes larger. Consistently, the droplets formed with an orifice of $AR = 8$ are larger than those with smaller AR, which is shown in Fig. 12. The experimentally obtained break-up lengths show increasing values upon increasing aspect ratio.

To investigate the capabilities of the numerical model to capture the axis-switching behavior, the numerically obtained jet oscillations are time-averaged and compared with the experimental results. These oscillations are shown in Figs. 14 and 15 where the outline of the jet is represented in a front and side view for the numerical (blue line) and experimental results (red line). This comparison shows that the position of the jet obtained numerically lies within the experimental error margin for all the studied conditions. Additionally, axis-switching is clear for both experiments and simulations as the observed jet expansions and contractions alternate in the front and side view. Particularly, an excellent agreement is observed between experiments and simulations in the wavelengh of the first oscillation λ_1, as demonstrated in Fig. 16 where numerically and experimentally obtained values of λ_1 are compared in a parity plot. However, the amplitude of the numerically obtained oscillations with $AR = 5$ (see Fig. 14) deviates slightly from the experiments, which could be caused by external experimental conditions that are not represented in the model, such as vibrations or the presence of contaminants in the liquid phase.

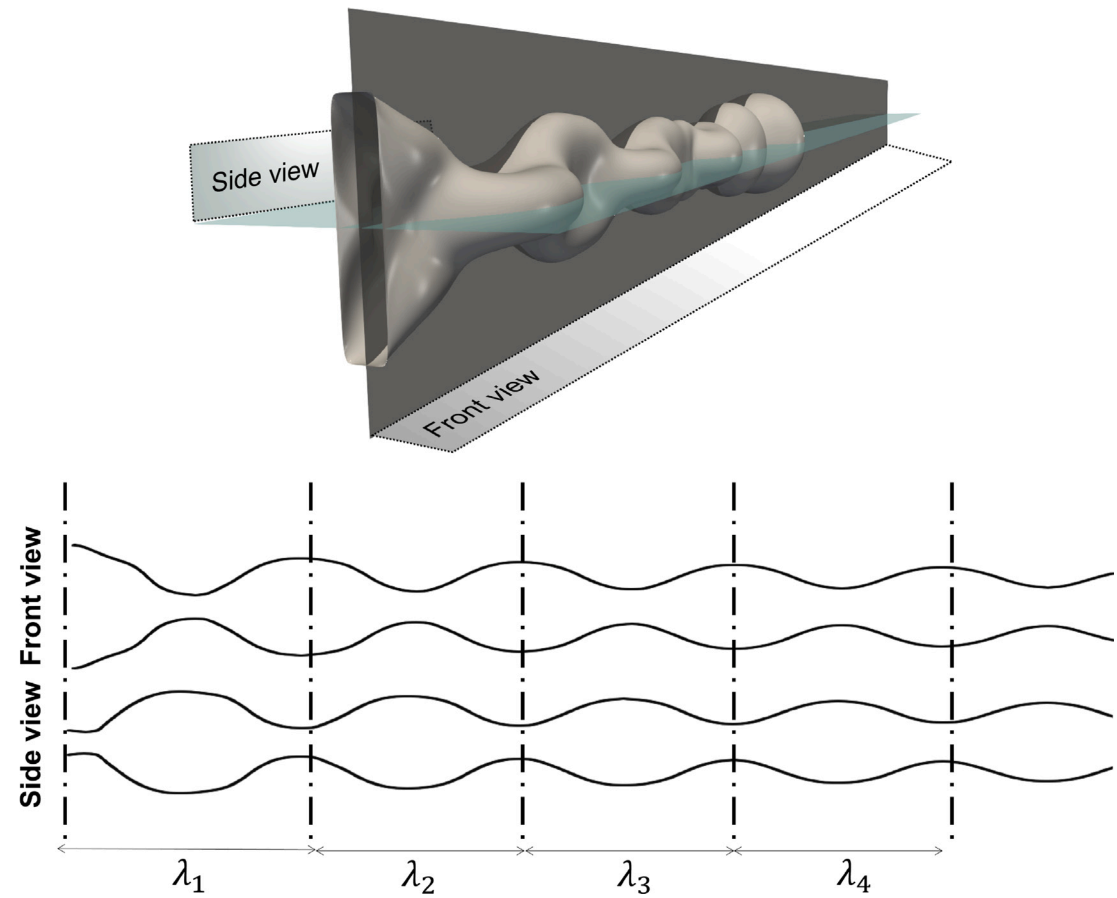

Fig. 10. Example of axis-switching behavior in one of the simulations, top view; a 3D surface plot of the rectangular jet, bottom view; a side and front view of the outline of the surface.

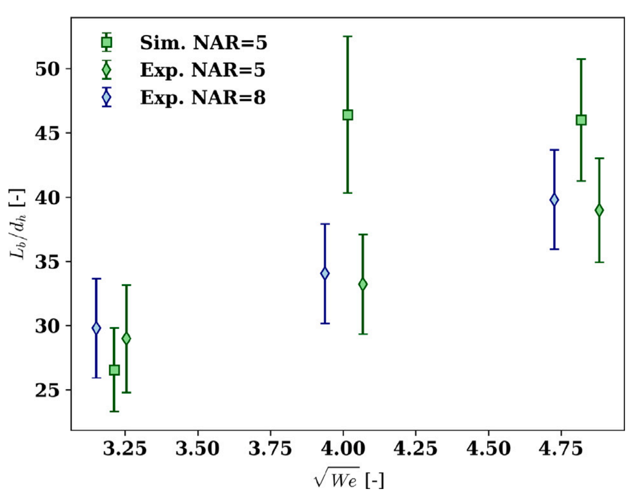

Fig. 11. Break-up length versus Weber number.

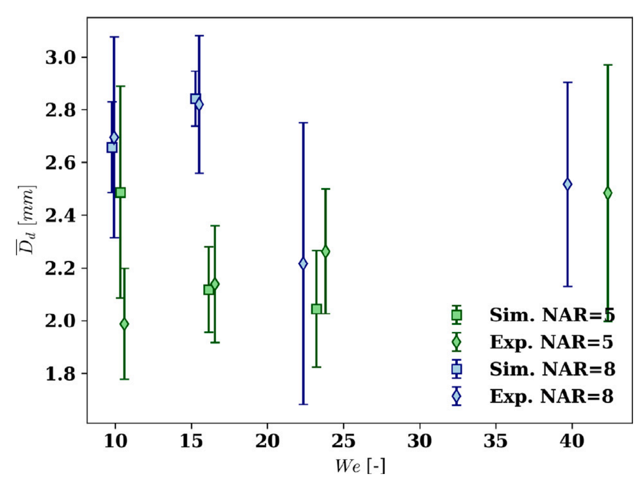

Fig. 12. Droplet size versus Weber number.

5.2. Velocity relaxation effect

After the jet is discharged, the non-slip boundary condition at the nozzle wall changes to a free slip condition, which forces the velocity profile of the jet to become flat. If the length of the nozzle is long enough, a fully develop flow is generated at the nozzle outlet. This velocity profile relaxes towards a flat profile upon injection due to the altered lateral stress profile. The associated momentum transfer leads to kinetic energy redistribution between the jet transverse layers. In the Rayleigh regime, a flat velocity profile exerts a destabilizing effect which leads to shorter break-up lengths in round jets (Ibrahim and Marshall, 2000). To evaluate the impact of velocity relaxation in a rectangular jet, simulations were performed with a fully developed profile given by Eq. (12) at the nozzle exit. Fig. 17 compares the break-up length values for a fully developed and a flat velocity profile at

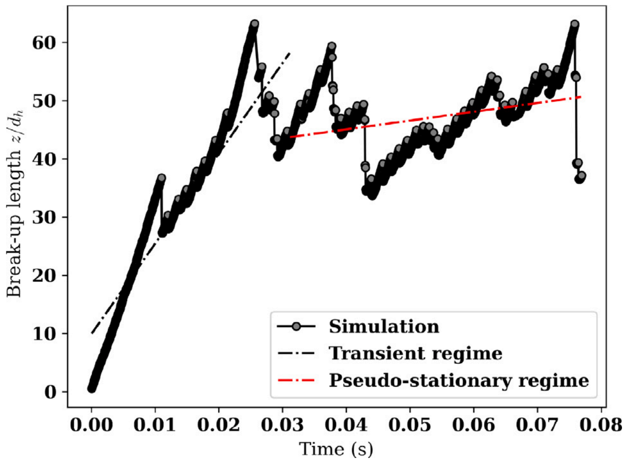

Fig. 13. Break-up length over time for Re = 1000 and AR = 5.

the same We and Re conditions. As evident from this graph, a fully developed profile enhances the stability of the jet causing higher break-up lengths compared to a uniform velocity profile. Additionally, axis switching is also observed for a fully developed profile where the length of the first oscillation (λ_1) is larger compared to the observations when a flat velocity profile is used, as shown in Fig. 18. Both Figs. 17 and 18 show a linear dependency with $\sqrt{We}$ for a flat velocity profile. In contrast, the break-up length and λ_1 at $\sqrt{We}$ = 4.8 and Re = 1200 deviates from the linear trend when a fully develop profile is imposed at the outlet, which could result from a transition to a different regime.

5.2.1. Axis-switching behavior

Axis-switching is the alternating expansion and contraction of the jet along the major and minor axes of the rectangular jet. As a result of this, the cross-section of the jet switches the major and minor axes along its main propagation direction. Thus, the jet oscillations in a front view parallel to the major axis of the jet will be in anti-phase with respect to the oscillations in a 90° rotated view, which is the behavior observed for both the fully developed and flat velocity profile at the nozzle outlet in Fig. 19. In this figure, the recirculations located at the crest of each jet oscillation are observed in the streamlines (see blue colored lines) and strong radial components of the velocity field (see deep blue and red color in the top half of the front and side views). These recirculations lead to flow entrainment and pressures gradients, causing a pressure drop at the central point of the oscillation where the recirculation converges. The flow entrainment, evidenced in the recirculations in Fig. 19, originates from the self-induced Biot–Savart deformation of vortex rings and the interaction between azimuthal and stream-wise vorticity according to Gutmark and Grinstein (1999). Fig. 20 shows the iso-contours of azimuthal and stream-wise vorticity around the jet at different progressing times. This figure shows the formation of vortical structures that persist in time. Additionally, the azimuthal and stream-wise vortices intersect in the regions where the jet cross section rotates.

The interaction of the azimuthal and stream-wise vortices are enhancing the mass entrainment (Gutmark and Grinstein, 1999). To characterize the mass entrainment, we use the definition of Crow and Champagne (1971) and Liepmann and Gharib (1992), who define the local entrainment rate as the partial derivative of the radial volume flux, as shown in Eq. (13).

$$\frac{\partial(Q/Q_0)}{\partial(z/d_h)} = \frac{d_h}{Q_0}\oint_c \mathbf{u}\cdot\hat{\mathbf{n}}\,d\tau = \frac{d_h}{Q_0}\int_0^{2\pi} u_r\, r\, d\theta, \tag{13}$$

where c is the contours of the jet cross-section in this case and Q_0 the volumetric flow rate at the nozzle outlet.

Fig. 21 shows the entrainment rate at various stream-wise positions, where we can observe that it becomes steady when $t^* > 21.6$. The negative and positive values in this curve, represent the entrainment towards the inside and outside of the jet, respectively. It should be noted that this profile will vary depending on the integration path chosen to solve Eq. (13). To evaluate the impact on the entrainment rate of the velocity profile, we represent the entrainment rate in Fig. 22. As evident from these graphs, a flat velocity profile at the nozzle outlet leads to more flow entrainment compared to a poiseuille-like velocity profile, particularly, in the region close to the nozzle outlet. Additionally, the difference between the flow entrainment in the fully developed and flat velocity profile decreases with increasing values of injection velocity, which suggests that stream-wise inertia forces outbalance the effect of the vortical structures.

Nomenclature

Notation		
Symbol	Description	Unit
Re	Reynolds number	[–]
We	Weber number	[–]
Oh	Ohnesorge number	[–]
AR	Aspect ratio	[–]
d_s	Small nozzle diameter	μm
d_b	Big nozzle diameter	μm
d_h	Hydraulic diameter	μm
$L_{dev.}$	Nozzle length	μm
U_0	Average fluid velocity	m/s
μ	Dynamic viscosity	kg/(m s)
ν	Kinematic viscosity	m^2/s
ρ	Density	kg/m^3
σ	Surface tension	N/m
$\mathbf{u}$	Velocity	m/s
$\mathbf{g}$	Gravity force	m/s^2
τ	Stress tensor	N/m^2
p	Pressure	N/m^2
$\mathbf{F}_\sigma$	Volumetric surface tension force	N/m^3
p	Pressure	N/m^2
t	Time	s
Δx	Grid spacing	m
Δt	Time step	s
r	Droplet radius	m
L_b	Break-up length	m
λ	Wavelength	m
Q	Volume flux	m^3/s
w	Vorticity	s^{-1}

Subscripts and superscripts	
Symbol	Description
l	Liquid phase
g	Gas phase
x	x direction
y	y direction
z	z direction
r	Radial direction
θ	Azimuth direction

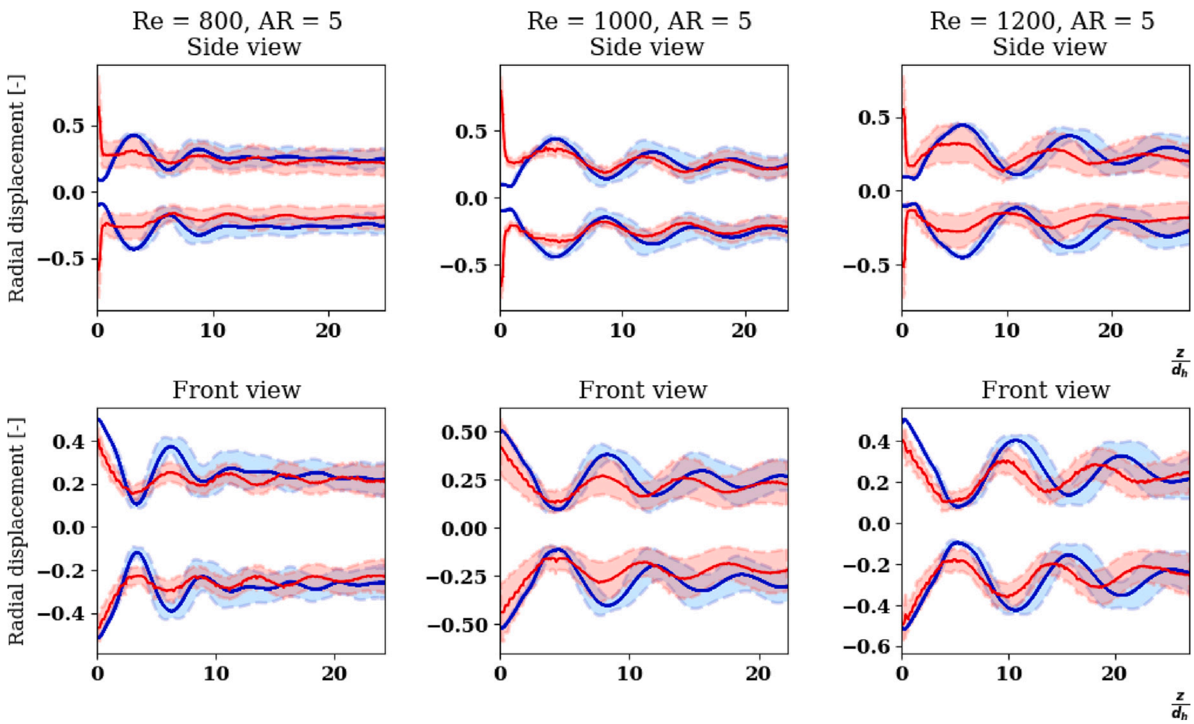

Fig. 14. Outline (continuous line) representing the averaged position of the jet with AR = 5 and the standard deviation represented with a shaded area. The red color refers to experiments, while blue color represents simulations. (For interpretation of the references to color in this figure legend, the reader is referred to the web version of this article.)

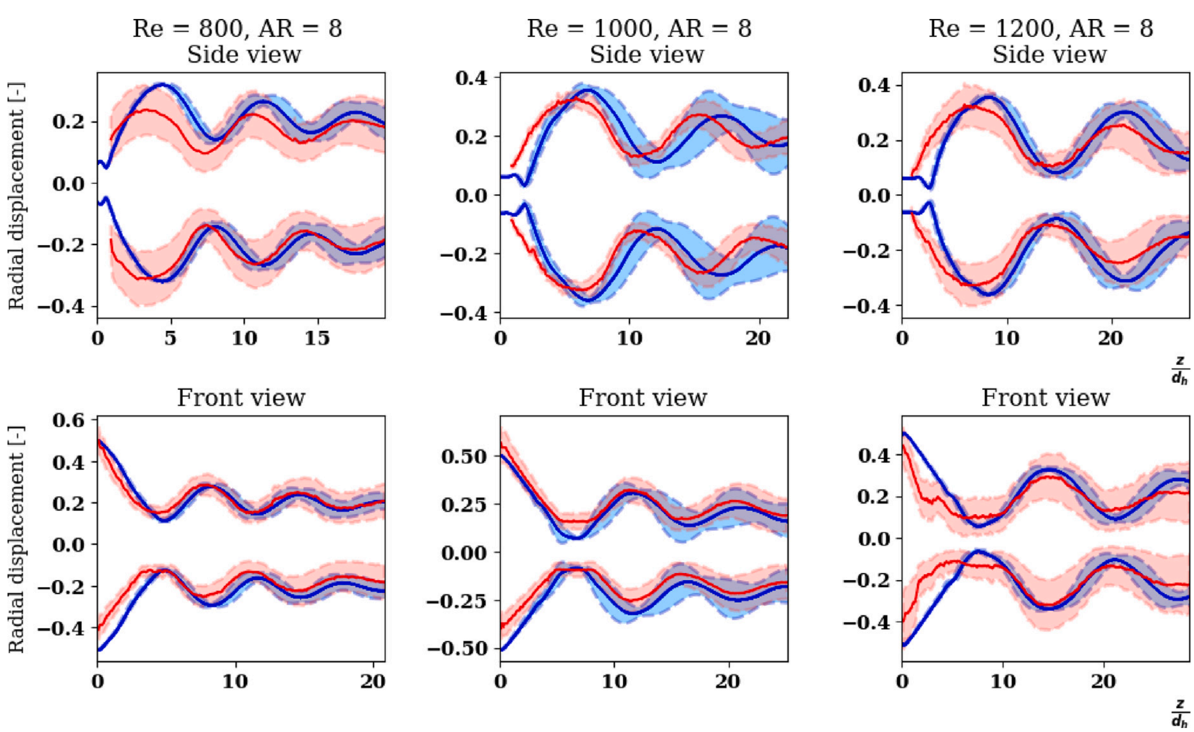

Fig. 15. Outline (continuous line) representing the averaged position of the jet with AR = 8 and the standard deviation represented with a shaded area. The red color refers to experiments, while blue color represents simulations. (For interpretation of the references to color in this figure legend, the reader is referred to the web version of this article.)

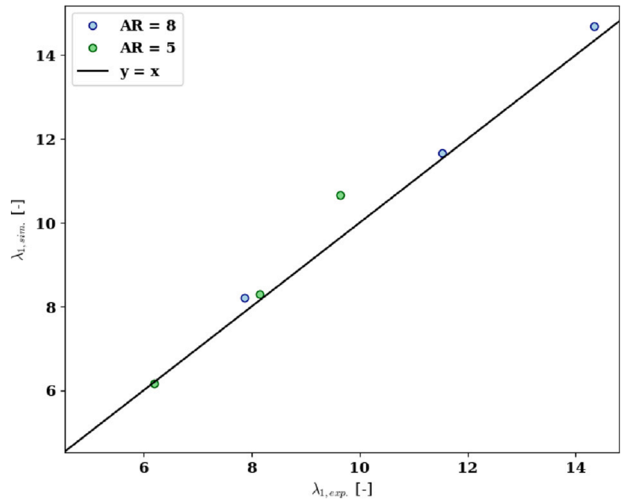

Fig. 16. Parity plot where λ_1 is compared between simulations $\lambda_{1,sim.}$ and experiments $\lambda_{1,exp.}$.

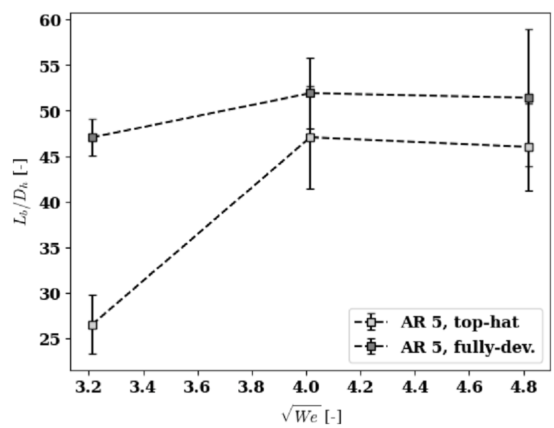

Fig. 17. Break-up length of a rectangular jet of $AR = 5$ with a fully developed and flat velocity profile at the nozzle outlet for various We conditions corresponding to $Re = 800, 1000$ and 1200. The error bars indicate the standard deviation.

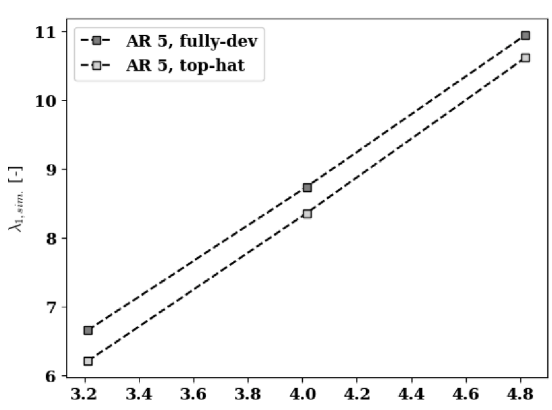

Fig. 18. Wavelength λ_1 of a rectangular jet of $AR = 5$ with a fully developed and flat velocity profile at the nozzle outlet for various We conditions corresponding to $Re = 800, 1000$ and 1200.

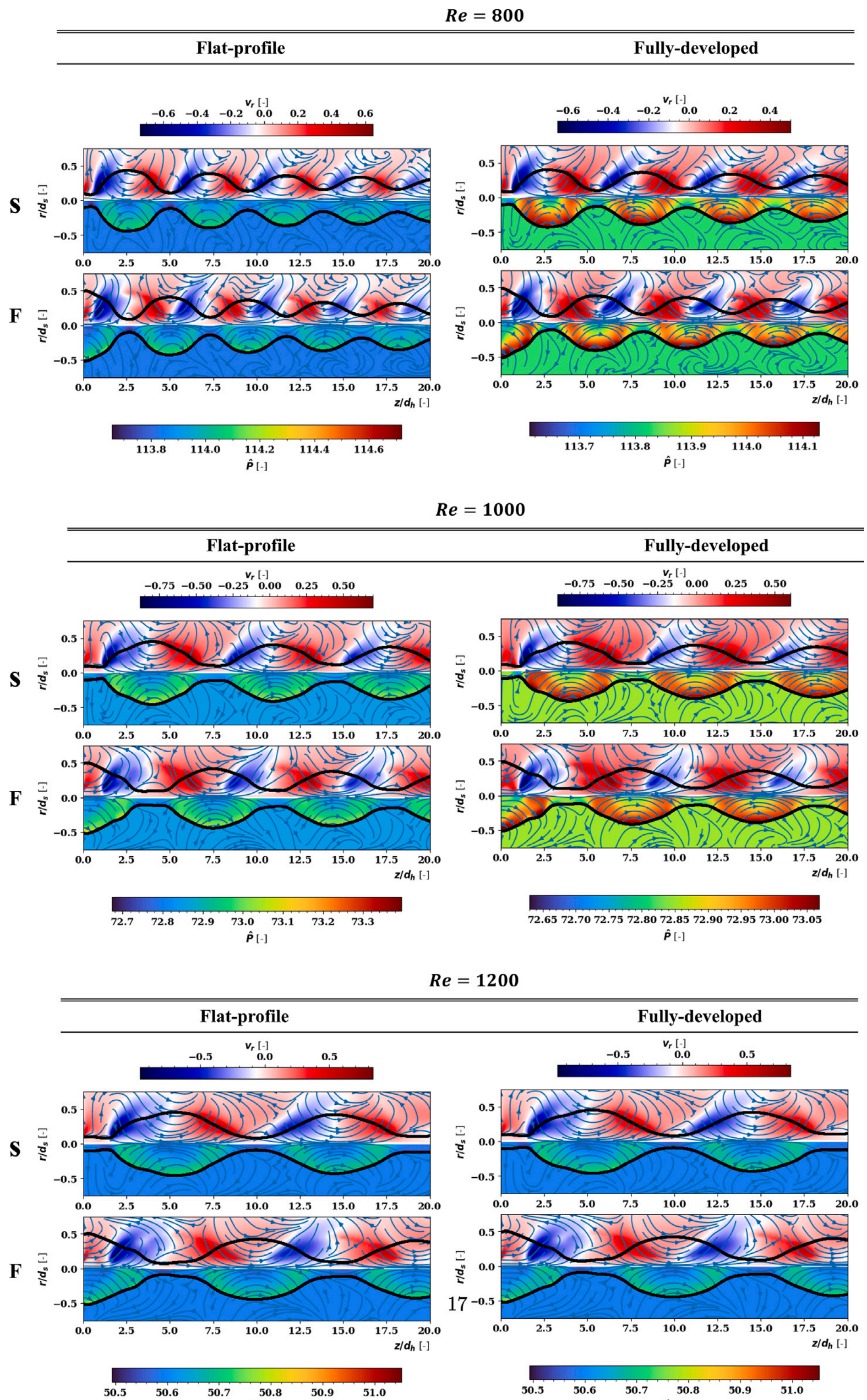

Fig. 19. Streamlines, radial velocity (top half) and pressure field (bottom half) are shown at a front (F) and side (S) slice for fully develop and flat velocity profile. (For interpretation of the references to color in this figure legend, the reader is referred to the web version of this article.)

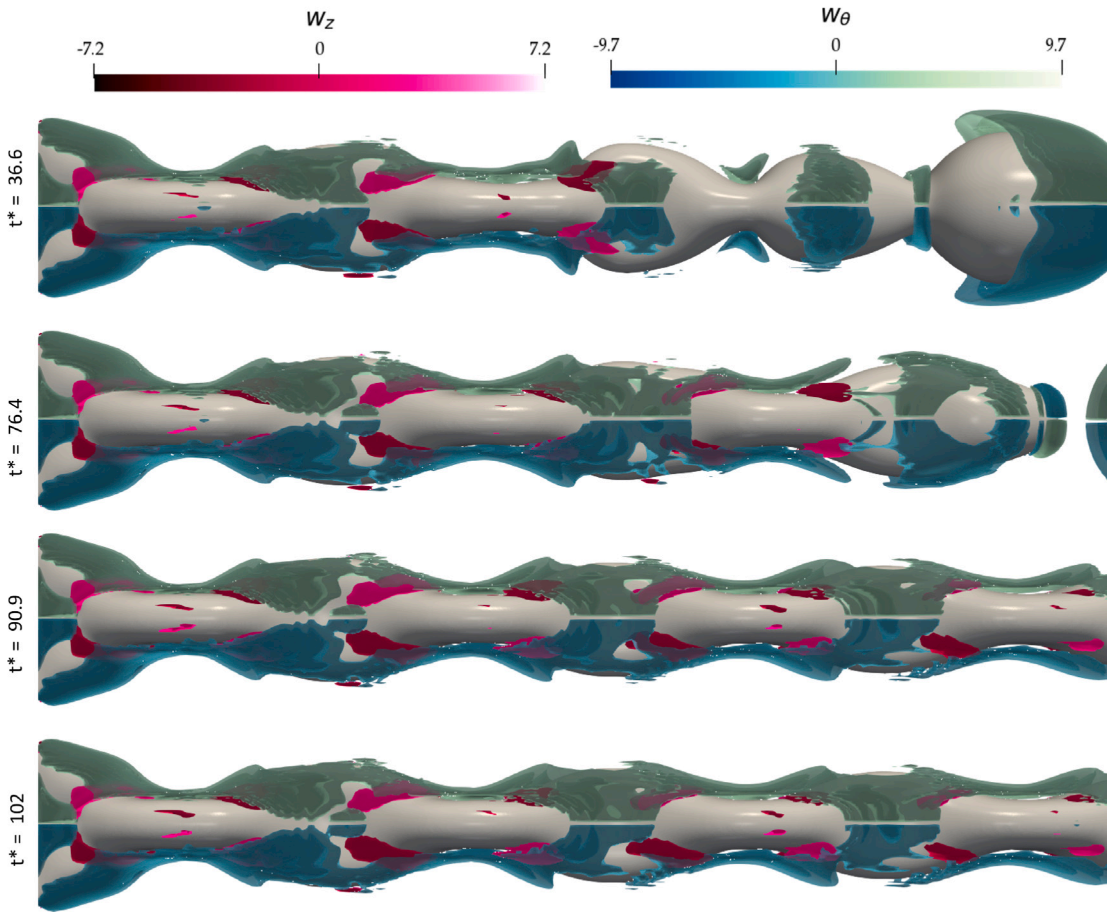

Fig. 20. Jet and iso-contours of stream-wise w_z and azimuthal vorticity w_θ at different progressing times t^* corresponding with the simulation case at Re = 800 and a fully developed profile.

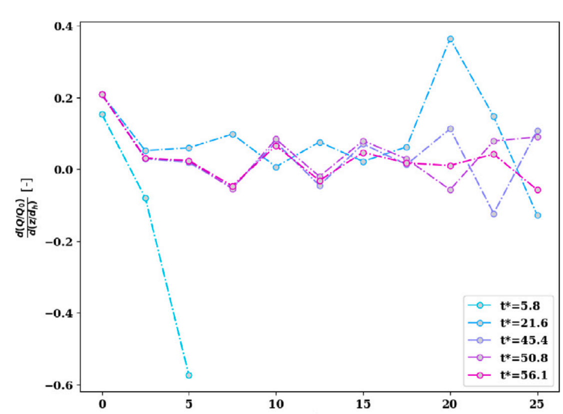

Fig. 21. Entrainment rate corresponding to the case with Re = 800, AR = 5, and a flat velocity profile.

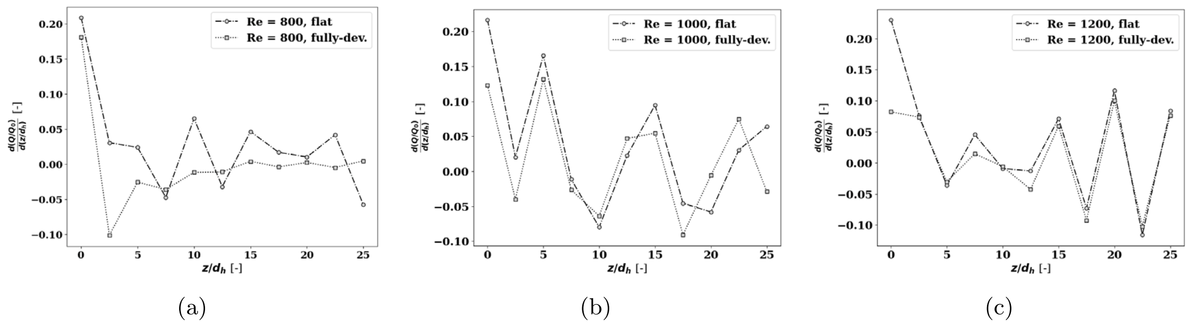

Fig. 22. Entrainment rate for (a) Re = 800, (b) Re = 1000, (c) Re = 1200. The figures show both fully developed and flat velocity profile at the nozze outlet.

CRediT authorship contribution statement

C. García Llamas: Writing – original draft, Visualization, Validation, Software, Methodology, Investigation, Formal analysis, Data curation, Conceptualization. **V.V. Swami:** Writing – original draft, Visualization, Validation, Formal analysis, Data curation, Conceptualization. **V.P. Petrova:** Formal analysis, Data curation, Conceptualization, Writing – review & editing. **K.A. Buist:** Writing – review & editing, Supervision, Methodology, Funding acquisition. **J.A.M. Kuipers:** Writing – review & editing, Supervision, Project administration, Methodology, Funding acquisition. **M.W. Baltussen:** Writing – review & editing, Supervision, Project administration, Funding acquisition, Formal analysis, Data curation, Conceptualization.

Declaration of competing interest

The authors declare the following financial interests/personal relationships which may be considered as potential competing interests: M.W. Baltussen, K.A. Buist and J.A.M. Kuipers reports financial support was provided by TKI Energy. M.W. Baltussen, K.A. Buist and J.A.M. Kuipers reports financial support was provided by DSM. M.W. Baltussen, K.A. Buist and J.A.M. Kuipers reports financial support was provided by Royal FrieslandCampina. M.W. Baltussen, K.A. Buist and J.A.M. Kuipers reports financial support was provided by Danone. If there are other authors, they declare that they have no known competing financial interests or personal relationships that could have appeared to influence the work reported in this paper.

Data availability

Data will be made available on request.

Acknowledgments

This work is part the “EEMS - Energy Efficient Milky Sprays” project which took place within the framework of the Institute of Sustainable Process Technology (ISPT) and was co-financed by the TKI-Energy & Industry, Danone, DSM-firmenich and FrieslandCampina. More information can be found at the EEMS website. We thank the High-Performance Computing Service Snellius for their computational resources and support.

References

Amini, G., Dolatabadi, A., 2011. Capillary instability of elliptic liquid jets. Phys. Fluids 23 (8), 084109, arXiv:https://pubs.aip.org/aip/pof/article-pdf/doi/10.1063/1.3626550/15735446/084109_1_online.pdf.

Amini, G., Dolatabadi, A., 2012. Axis-switching and breakup of low-speed elliptic liquid jets. Int. J. Multiph. Flow 42, 96–103.

Bidone, G., 1829. Expériences Sur La Forme Et Sur La Direction Des Veines Et Des Courans [Sic] D'eau Lancés Par Diverses Ouvertures. Imprimerie royale.

Brackbill, J.U., Kothe, D.B., Zemach, C., 1992. A continuum method for modeling surface tension. J. Comput. Phys. 100 (2), 335–354.

Carrillo, J.M., Marco, F., Castillo, L.G., García, J.T., 2021a. Experimental study of submerged hydraulic jumps generated downstream of rectangular plunging jets. Int. J. Multiph. Flow (ISSN: 0301-9322) 137, 103579. http://dx.doi.org/10.1016/j.ijmultiphaseflow.2021.103579, URL https://www.sciencedirect.com/science/article/pii/S0301932221000276.

Carrillo, J.M., Ortega, P.R., Castillo, L.G., García, J.T., 2021b. Air–water properties in rectangular free-falling jets. Water (ISSN: 2073-4441) 13 (11), http://dx.doi.org/10.3390/w13111593, URL https://www.mdpi.com/2073-4441/13/11/1593.

Castillo, L.G., Carrillo, J.M., Blázquez, A., 2015. Plunge pool dynamic pressures: A temporal analysis in the nappe flow case. J. Hydraul. Res. (ISSN: 00221686) 53, http://dx.doi.org/10.1080/00221686.2014.968226.

Castillo, L., Puertas, J., Dolz, J., 1999. Pressure fluctuations on plunge pool floors. J. Hydraul. Res. (ISSN: 0022-1686) 37, http://dx.doi.org/10.1080/00221689909498311.

Chen, N., Yu, H., 2014. Mechanism of axis switching in low aspect-ratio rectangular jets. Comput. Math. Appl. 67 (2), 437–444.

Chorin, A., 1968. Numerical solution of the Navier-Stokes equations. Math. Comp. 22, 745–762.

Crow, S.C., Champagne, F.H., 1971. Orderly structure in jet turbulence. J. Fluid Mech. 48 (3), 547–591.

Deen, N.G., Van Sint Annaland, M., Kuipers, J.A.M., 2004. Multi-scale modeling of dispersed gas–liquid two-phase flow. Chem. Eng. Sci. 59 (8), 1853–1861, Complex Systems and Multi-scale Methodology.

Dijkhuizen, W., Roghair, I., Van Sint Annaland, M., Kuipers, J.A.M., 2010. DNS of gas bubbles behaviour using an improved 3D front tracking model—Drag force on isolated bubbles and comparison with experiments. Chem. Eng. Sci. 65 (4), 1415–1426.

Eggers, J., Villermaux, E., 2008. Physics of liquid jets. Rep. Progr. Phys. 71 (3), 036601.

Farvardin, E., Dolatabadi, A., 2013. Numerical simulation of the breakup of elliptical liquid jet in still air. J. Fluids Eng. 135 (7), 071302, arXiv:https://asmedigitalcollection.asme.org/fluidsengineering/article-pdf/135/7/071302/6188755/fe_135_7_071302.pdf.

Gutmark, E.J., Grinstein, F.F., 1999. Flow control with noncircular jets. Annu. Rev. Fluid Mech. 31 (1), 239–272, arXiv:https://doi.org/10.1146/annurev.fluid.31.1.239.

Ho, C.-M., Gutmark, E., 1987. Vortex induction and mass entrainment in a small-aspect-ratio elliptic jet. J. Fluid Mech. 179, 383–405.

Husain, H.S., Hussain, A.K.M.F., 1983. Controlled excitation of elliptic jets. Phys. Fluids 26 (10), 2763–2766.

Husain, H.S., Hussain, F., 1993. Elliptic jets. Part 3. Dynamics of preferred mode coherent structure. J. Fluid Mech. 248, 315–361.

Ibrahim, E., Marshall, S., 2000. Instability of a liquid jet of parabolic velocity profile. Chem. Eng. J. 76 (1), 17–21.

Jaberi, A., Tadjfar, M., 2019. Wavelength and frequency of axis-switching phenomenon formed over rectangular and elliptical liquid jets. Int. J. Multiph. Flow 119, 144–154.

Kasyap, T., Sivakumar, D., Raghunandan, B., 2009. Flow and breakup characteristics of elliptical liquid jets. Int. J. Multiph. Flow 35 (1), 8–19.

Koshigoe, S., Gutmark, E., Schadow, K.C., Tubis, A., 1989. Initial development of noncircular jets leading to axis switching. AIAA J. 27 (4), 411–419.

Kuprat, A., Khamayseh, A., George, D., Larkey, L., 2001. Volume conserving smoothing for piecewise linear curves, surfaces, and triple lines. J. Comput. Phys. 172, 99–118.

Lekic, N., Birouk, M., 2009. Liquid jet breakup in quiescent atmosphere: A review. Atom. Sprays (ISSN: 1044-5110) 19 (6), 501–528.

Liepmann, D., Gharib, M., 1992. The role of streamwise vorticity in the near-field entrainment of round jets. J. Fluid Mech. 245, 643–668.

Magnus, G., 1855. Hydraulische untersuchungen. Ann. Phys., Lpz. 171 (5), 1–59, arXiv:https://onlinelibrary.wiley.com/doi/pdf/10.1002/andp.18551710502.

Masterov, M., 2019. Towards industrial-scale bubble columns: the development and application of the high performance computing framework (Ph.D. thesis). Chemical Engineering and Chemistry, ISBN: 978-90-386-4938-2, Proefschrift.

McCarthy, M., Molloy, N., 1974. Review of stability of liquid jets and the influence of nozzle design. Chem. Eng. J. 7 (1), 1–20, An International Journal of Research and Development.

Morad, M.R., Nasiri, M., Amini, G., 2020. Axis-switching and breakup of rectangular liquid jets. Int. J. Multiph. Flow 126, 103242.

Rayleigh, L., 1878. On the instability of jets. In: Proc Lond Math Soc. Vol. 10, pp. 4–13.

Rayleigh, L., et al., 1879. On the capillary phenomena of jets. Proc. R. Soc. Lond. 29 (196–199), 71–97.

Reitz, R., Bracco, F., 1986. Mechanisms of breakup of round liquid jets. Ency. Fluid Mech. 3.

Shin, S., Abdel-Khalik, S.I., Daru, V., Juric, D., 2011. The Local Front Reconstruction Method for direct simulation of two- and three-dimensional multiphase flows. J. Comput. Phys..

Straccia, J.C., Farnsworth, J.A.N., 2021. Axis switching in low to moderate aspect ratio rectangular orifice synthetic jets. Phys. Rev. Fluids 6, 054702.

Tadjfar, M., Jaberi, A., 2019. Effects of aspect ratio on the flow development of rectangular liquid jets issued into stagnant air. Int. J. Multiph. Flow 115, 144–157.

Trilinos Project Team, T., 2020. The trilinos project website.

Van Sint Annaland, M., Deen, N.G., Kuipers, J.A.M., 2005. Numerical simulation of gas bubbles behaviour using a three-dimensional volume of fluid method. Chem. Eng. Sci. 60 (11), 2999–3011.

Versteeg, H.K., Malalasekera, W., 1995. An Introduction to Computational Fluid Dynamics - the Finite Volume Method. I–X, Addison-Wesley-Longman, ISBN: 978-0-582-21884-0, pp. 1–257.

Wang, C., 2009. Heat transfer and flow through a super-elliptic duct – Effect of corner rounding. Mech. Res. Commun. 36 (4), 509–514.

Wang, F., Fang, T., 2015. Liquid jet breakup for non-circular orifices under low pressures. Int. J. Multiph. Flow 72, 248–262.